Wiley Online Library
Early View publication on www.wileyonlinelibrary.com
(issue and page numbers not yet assigned;
citable using Digital Object Identifier – DOI)

J. Biophotonics 1–11 (2016) / **DOI** 10.1002/jbio.201600050

Journal of BIOPHOTONICS

FULL ARTICLE

Wide-field time-gated photoluminescence microscopy for fast ultrahigh-sensitivity imaging of photoluminescent probes

Wan A. W. Razali[1, 2, 3], *Varun K. A. Sreenivasan*[1, 3], *Carlo Bradac*[4], *Mark Connor*[5], *Ewa M. Goldys*[1, 3], *and Andrei V. Zvyagin*[*, 1, 3, 6]

[1] MQ Photonics Research Centre, Faculty of Science, Macquarie University, Sydney, NSW 2109, Australia
[2] Department of Physics, Faculty of Applied Sciences, Universiti Teknologi MARA Pahang, 26400 Jengka, Pahang, Malaysia
[3] ARC Centre of Excellence for Nanoscale BioPhotonics (CNBP), Macquarie University, Sydney, NSW 2109, Australia
[4] ARC Centre of Excellence for Engineered Quantum Systems (EQuS), Department of Physics and Astronomy, Macquarie University, Sydney, NSW 2109, Australia
[5] Department of Biomedical Sciences, Faculty of Medicine and Health Sciences, Macquarie University, Sydney, NSW 2109, Australia
[6] Laboratory of Optical Theranostics, N.I. Lobachevsky Nizhny Novgorod State University, 603950 Nizhny Novgorod, Russia

Received 22 February 2016, revised 12 May 2016, accepted 13 May 2016
Published online 7 June 2016

Key words: Imaging, nanoruby, time-gated detection, photoluminescence, sensitivity, autofluorescence, background suppression

Fluorescence microscopy is a fundamental technique for the life sciences, where biocompatible and photostable photoluminescence probes in combination with fast and sensitive imaging systems are continually transforming this field. A wide-field time-gated photoluminescence microscopy system customised for ultrasensitive imaging of unique nanoruby probes with long photoluminescence lifetime is described. The detection sensitivity derived from the long photoluminescence lifetime of the nanoruby makes it possible to discriminate signals from unwanted autofluorescence background and laser backscatter by employing a time-gated image acquisition mode. This mode enabled several-fold improvement of the photoluminescence imaging contrast of discrete nanorubies dispersed on a coverslip. It enabled recovery of the photoluminescence signal emanating from discrete nanorubies when covered by a layer of an organic fluorescent dye, which were otherwise invisible without the use of spectral filtering approaches. Time-gated imaging also facilitated high sensitivity detection of nanorubies in a biological environment of cultured cells. Finally, we monitor the binding kinetics of nanorubies to a functionalised substrate, which exemplified a real-time assay in biological fluids.

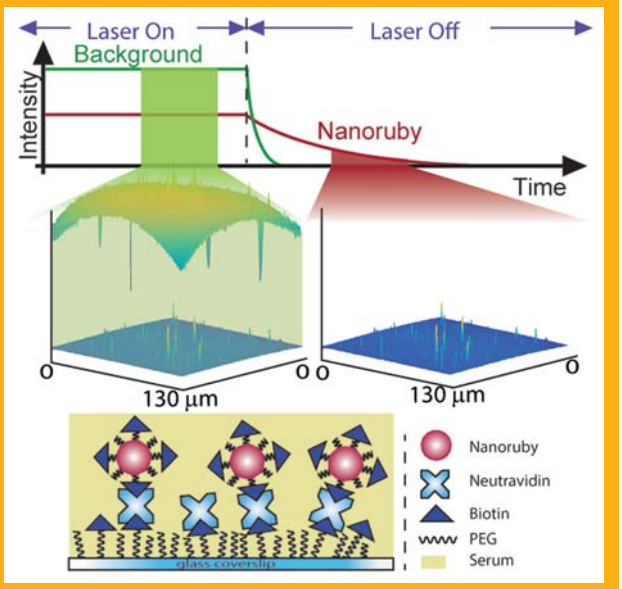

3D-pseudo colour images of nanorubies immersed in a highly fluorescent dye solution. Nanoruby photoluminescence is subdued by that of the dye in continuous excitation/imaging (left), however it can be recovered by time-gated imaging (right). At the bottom is schematic diagram of nanoruby assay in a biological fluid.

* Corresponding author: e-mail: andrei.zvyagin@mq.edu.au, Phone: +61-2-9850-7760, Fax: +61-2-9850-8115

1. Introduction

Labelling of biological molecules with fluorescence probes (more generally, photoluminescence probes) enables molecularly-specific, morphological and functional imaging. This has become an indispensable tool in modern biomedical research and practices [1–3]. Advances in optical imaging techniques and photoluminescence (PL) probes have enabled the development of fluorescence microscopy towards more rapid, sensitive and selective imaging.

Traditional PL probes based on organic dyes suffer from several drawbacks, such as photobleaching, broad emission spectrum, non-specific chemical reactivity and poor chemical stability [4–6], which limit the scope of their application towards ultrahigh-sensitivity and single-molecule imaging [7]. There is continuing interest in developing alternative PL probes. Fluorescent carbon dots [8], metal nanoclusters [9, 10] plasmonic nanoparticles, upconversion nanoparticles [11] and nanorubies [12] are some of the newly developed PL probes. They exhibit exceptional optical and physicochemical properties, such as virtually unlimited photostability, chemical stability and colloidal stability. Such PL probes have revolutionised fluorescence imaging by introducing modalities such as super-resolution microscopy using fluorescent nanodiamonds [13], in vivo optical imaging using upconversion nanoparticles [14], and time-gated microscopy using photoluminescent nanomaterials [12].

The time-gated detection makes use photoluminescent millisecond-scale emission, and is realised by turning on a photoreceiver, following a short time delay after the excitation source is ended. The ability to discriminate probes with long PL lifetime from obscuring, but more rapidly decaying optical background gives time-gated microscopy a competitive edge over other methods. It is particularly advantageous when the optical background is such that spectral and other filtering methods are insufficient, as is the case for biological autofluorescence. The time-gated photoluminescence (TGP) detection concept is presented in Figure 1. The signal from a PL probe is acquired only after the intrinsic fluorescence of biological matter (autofluorescence) has decayed. The effectiveness of this technique generally improves when the PL lifetimes of the probe, τ_{PL}, greatly exceeds that of the autofluorescence, τ_{AF}. A gate time, Δt between the excitation pulse trailing edge and the onset of the emission signal acquisition is therefore set to satisfy the condition: $\tau_{AF} \ll \Delta t \ll \tau_{PL}$. Typical values of the emission lifetime range from tens of picoseconds [15] to several nanoseconds [16, 17] for τ_{AF}; and from hundreds of microseconds [18] to milliseconds [12] for τ_{PL}. The TGP method (also termed "time-gated luminescence (TGL)" elsewhere) was applied extensively for high-sensitivity PL probe imaging [19] of cancer cells [20–22] and pathogens [23, 24]. In this paper, we used "photoluminescence" term because it is more accurately describes the phenomenon. The term "luminescence" is prone to misinterpretation with bioluminescence or chemiluminescence which is used in the field of biology [25].

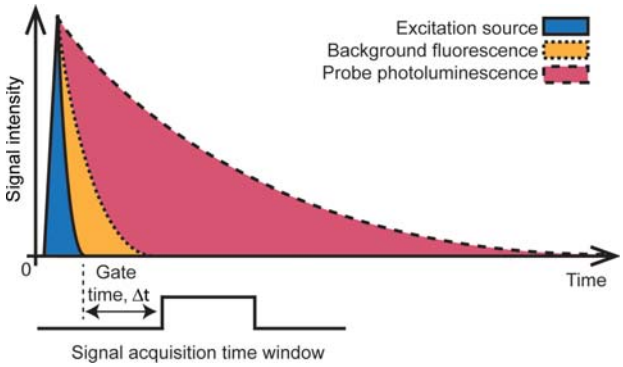

Figure 1 Conceptual illustration of normalised temporal profiles of three main optical signals (excitation, autofluorescence, probe photoluminescence) relevant to the time-gated photoluminescence imaging.

In our earlier work [12], we used a home-built confocal fluorescence system to attain high sensitivity imaging of nanorubies. However, this system was inherently limited in the imaging acquisition rate. The long photoluminescence lifetime of nanoruby (τ_{NR}), demanded dwelling over each pixel for times longer than τ_{NR}. Therefore, it required approximately 30 min to acquire one image sized 1024×1024 pixels. Other reported TGP techniques can either be classified as sensitive or rapid, but not both. For example, Connally et al. demonstrated the suppression of the autofluorescent background to emphasise europium-chelate labelled prokaryotic parasites using time-resolved wide-field photoluminescence microscopy [26]. Even though their acquisition rate was very fast (25 frames per second), their sensitivity fell short from that required for studying single molecular events. Other TGP schemes featuring modest imaging sensitivities includes work by Bouccara et al., where the acquisition time of 0.15 s per image was demonstrated [27]. The fastest TGP scheme featuring single-particle sensitivity was reported by Zhang et al., and demonstrated the acquisition time of 30 s per frame [23]. Another way of increasing sensitivity without compromising on acquisition speed is by employing probes of high brightness. For example, tracking of single neurotransmitter receptors has been carried out with quantum dots as the labelling agent [28]. However, these advantages present drawbacks of cytotoxicity and blinking as well as poor contrast in a biological

environment with high levels of autofluorescence background.

Here, we report a time-gated photoluminescence system, which enables fast imaging (>0.3 Hz) of individual photoluminescent nanoparticles, suitable to visualise molecular trafficking in cells and biological fluids. We demonstrate the system performance by imaging nanoruby (α-Al_2O_3 nanocrystals doped with Cr^{3+}). Cr^{3+} ions give rise to the nanoruby photoluminescence, which is characterised by long emission lifetime (3.7 ms). Complete recovery of discrete nanorubies from the background fluorescence of a substrate, a highly fluorescent dye and an autofluorescent biological environment is demonstrated, without any compromise on the imaging rate/sensitivity. Finally, we exemplify a single molecule kinetic binding assay by a avidin-biotin system, where the kinetics of nanoruby binding is monitored in a biological fluid.

2. Experimental

2.1 Nanoruby production

Synthetic ruby crystals with dimension approximately 7 cm × 2 cm × 1 cm (Henan Union Abrasive Corp, China) were crushed using a hydraulic press (Enerpac, US) and sieved through a 63 μm metal sieve. Dynamic light scattering (DLS, Mastersizer 2000, Malvern Instruments) measurements showed that the size of the produced microrubies varied from 1 – 100 μm. This microruby powder was ball-milled to produce nanorubies by using an established protocol for producing nanoalumina [29].

2.2 Characterisation of nanoruby size and photoluminescence

15 mg of nanoruby powder was suspended in 1 mL Milli Q water and sonicated for 30 min followed by centrifugation for 5 min at 5000 × g. The supernatant devoid of large particles was collected and diluted 10 times in 1% (w/w) polyvinyl alcohol (PVA) for spin-coating. 20 μL of nanoruby in PVA was dropped on a copper grid adhered to a glass coverslip (borosilicate glass, BK7, Menzel Glaser) and spun for 100 s at 1500 rpm using a spin-coater (EC101D, Headway Research Inc.). The sample was imaged using a transmission electron microscope (TEM, Philips CM10) operating at an accelerating voltage of 100 keV.

Dilute nanoruby sample devoid of large particles was prepared in Milli Q water for colloidal size and fluorescence characterisation. The mean hydrodynamic diameter and colloidal dispersion were determined using DLS (Zetasizer NS, Malvern Instruments). The excitation and emission spectra of sample placed in a quartz cuvette (Starna Pty. Ltd., 10 mm path length) were measured using a spectrofluorometer (Fluorolog Tau3, JY Horiba).

2.3 The time-gated photoluminescence (TGP) microscopy system

The system was developed based on an inverted microscope (Olympus IX71) platform, as shown schematically in Figure 2a. Either an external 405 nm laser (TG_405_1.1, Quantitative Ltd.) or 532 nm laser (FB-532-1000-FS-FS-1-1-ST, RGB Lase) source was coupled to an illumination port of the microscope using Köhler-type optical configuration to produce near-uniform illumination at the sample plane, as described elsewhere [30]. An oil-immersion objective lens (100×, NA 1.3, Olympus) was used for acquiring high-resolution images in bright-field, epi-luminescence and time-gated modes. The microscope was equipped with three interchangeable filter-sets (Semrock), specified in Table 1. The filter sets contained a laser-line filter, dichroic beam-splitter and long-pass (and band-pass) filters. Spectral character-

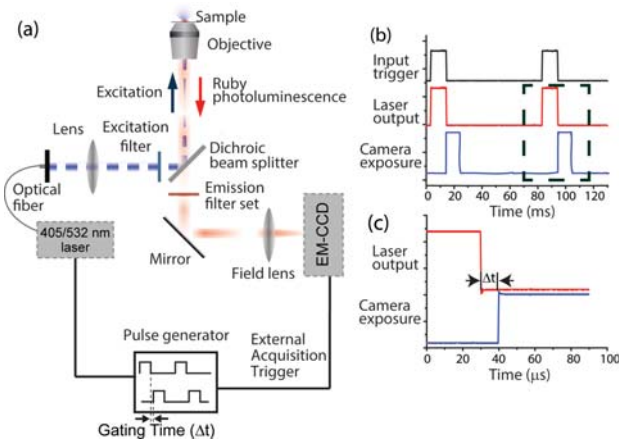

Figure 2 (**a**) A schematic diagram of the optical microscopy system configured for high-sensitivity imaging of nanoruby samples. A 405 nm/532 nm laser beam was coupled to the microscope to provide uniform illumination at the sample plane. The photoluminescence emission from the sample was collected through optical filters by using an EMCCD. The laser output and camera exposure were synchronised for TGP imaging. (**b**) Timing profiles of the input trigger signal, laser output and camera exposure during TGP imaging. (**c**) Magnified temporal sequence of the laser pulse and camera exposure (Δt stands for the gate time), for the region marked in (**b**) by a dashed rectangle.

Table 1 Optical filters used in this study.

Filter set #	Excitation filter	Dichroic mirror	Emission filter
1	650 nm SP*; FF01-650/SP-25	660 nm LP**; FF01-660/13-25	(a) 664 nm LP BLP01-664R-25 (b) 689 nm BP***; FF01-689/23-25
2	650 nm SP FF01-650/SP-25	660 nm LP FF01-660/13-25	(a) 664 nm LP BLP01-664R-25
3	–	511 nm LP FF511-Di01-25 × 36	450 nm LP

* SP = Short pass filter, ** LP = Long pass filter, *** BP = Band pass filter.

istics of filter set #1 are presented in Figure S1 (Supporting Information, SI). An electron-multiplied CCD camera (EMCCD, iXon 885 DU, Andor Technology Ltd.) was attached to a detection port of the microscope. TGP imaging was realised by synchronous operation of the electrically-modulated lasers and the EMCCD, as shown in Figure 2.

In the case of 405 nm laser, its inbuilt circuitry was used to modulate its output and for synchronization. The pulse width was set at 11 ms, three times longer than the PL lifetime of nanoruby (τ_{NR} = 3.7 ms), to allow steady-state excitation condition of Cr^{3+}. A short laser trailing edge time constant is crucial for TGP imaging. We ensured that this was much less than the gate time (Δt ~ 10 µs) to satisfy the condition $\tau_{AF} \ll \Delta t \ll \tau_{PL}$. A TTL output from the laser modulation circuit was used to trigger (input trigger in Figure 2b) a digital delay/dual pulse generator (DG535, Stanford Research System Inc, US). The DG535 generated a subsequent TTL pulse after a period of Δt ≈10 µs following the trailing edge of the laser pulse, which was used to trigger the EMCCD image acquisition (Figure 2c). The laser pulses were separated by ≈ 70 ms to accommodate for the time required for image acquisition and pixel readout.

When 532 nm laser was used, a field programmabale gate array (FPGA, NI PCIe-7841R Virtex-5, National Instruments) was used to synchronise the laser pulse and image acquisition. The FPGA was programmed to generate two TTL pulse trains, one to modulate the laser and another to trigger the EMCCD with flexible pulse durations, pulse separation and gating times (Δt).

The DG535 (via GPIB interface) and FPGA (via PCIe interface) were controlled via virtual instruments created using LabVIEW. The EMCCD camera was controlled by the Andor SOLIS software, version 4.22.

2.4 Characterisation of photoluminescence lifetime

65 µg of nanoruby was drop cast on a coverslip towards photoluminescence lifetime analysis with TGP using the 532 nm laser source (19 mW continuous optical power at sample plane, 10 ms pulse duration) and filter set #2. The gate time, Δt, was varied from 0.5 ms to 10 ms in 0.5 ms increments to cover the time scale of nanoruby photoluminescence. The exposure time was decremented by 0.5 ms between measurements to maintain the sum of exposure and gate times a constant, at 10 ms. An average pixel value was obtained for every measurement. The PL emission within every 0.5 ms time-window was defined as the difference between the pixel values of the subsequent measurements. τ_{NR} was estimated by fitting the time-dependent intensity to a single exponential function, $I(t) = I_0 \exp(-\Delta t/\tau_{NR})$ using Origin (OriginLab Corporation). Here, I_0 is the signal intensity at $\Delta t = 0$, which was used as a fitting parameter. Image analysis was performed using ImageJ (NIMH).

2.5 Correlative imaging

In order to correlate topography maps and photoluminescence images of discrete nanorubies, nanoruby aqueous colloid was drop-cast on a custom-made gridded coverslip and dried. Each 50 µm × 50 µm grid was tagged for easy identification, as described elsewhere [31]. The topography maps and TGP images were acquired by using an atomic force microscopy system (AFM, NT-MDT) and our home-built TGP system respectively. The peak height of the nanoparticles were directly obtained from the AFM data. The TGP image presented here was acquired with filter set #1 and 405 nm laser excitation with 11 ms pulses and imaged with 10 µs gating time, 100 accumulations and an EM gain of 100.

2.6 Charaterisation of TGP imaging sensitivity and contrast of discrete nanorubies

20 µL of nanoruby sample prepared in PVA (Section 2.2) was dropped on a square glass coverslip and spun for 100 s at 1500 rpm using a spin-coater. This coverslip was mounted on a glass slide and sealed with nail polish for PL (continuous excitation/detection and TGP) imaging. 405 nm laser was used at a power of 28 mW continuous power at the objective, with 11 ms pulse duration and 14% duty cycle. The electron-multiplication gain on the camera was

set to 100, and 40 frames, acquired at Δt varied from 0.3 µs to 1000 µs, were accumulated to obtain one image. The total time taken to generate an image was 3.2 s [40 × (11 ms laser pulse + 10 ms camera acquisition + 60 ms camera readout)]. The auto-photoluminescence background from empty glass- and quartz- slides and coverslips were also measured and analysed for evaluating background.

The imaging sensitivity of the microscope to detect individual nanorubies was determined by measuring the signal and background amplitudes expressed in terms of number of photons per second per pixel. In our experiments, the sensitivity was calculated using Weber contrast (C), which is defined as [32, 33]:

$$C = \frac{L_{max} - L_{min}}{L_{min}} \quad (1)$$

where L_{max} and L_{min} are PL maximum and minimum, respectively. In our case the L_{max} was equal to the sum of the signal and background, while L_{min} was the background. Therefore Eq. (1) was re-written for convenience in our case as:

$$C_{NR} = \frac{(S+B) - B}{B} \quad (2)$$

where, S is signal and B is background. S and B were calculated by averaging the brightest 10% and dimmest 10% of all pixels associated with each detected nanoruby spot, after correcting for camera offset using images acquired in the dark. In the case of complete suppression of the background, Eq. (2) reduces to $C_{NR} = S/N$, where N represents the EMCCD noise. Automated particle identification, intensity level measurements and contrast evaluation were carried out using image processing toolbox version 8.2 in Matlab R2013a or higher versions.

2.7 Nanoruby submerged in fluorescent dye

Nanoruby, devoid of large particles, were prepared as described earlier and mounted face-down on an ≈ 1 mm deep well on a glass slide made using nail polish. This well was pre-filled with 50 µL of a proprietary yellow fluorescent organic dye (L34959, Invitrogen), diluted 100 times using Milli Q water. Images of nanorubies excited by 405 nm laser were acquired in epi-luminescence and TGP modes with filter set #1. The laser power at the objective was set to 28 mW (continuous), with a pulse duration of 11 ms (14% duty cycle). The electron-multiplication gain on the camera was set to 50, accumulation to 40, and recursive average set to 5, and acquired at $\Delta t = 10$ µs.

2.8 Cell labelling and time-gated imaging

Mouse pituitary tumour cells (AtT-20) were cultured in DMEM (containing phenol red) supplemented with 10% FBS, 100 $\mu g \cdot mL^{-1}$ penicillin and 100 $\mu g \cdot mL^{-1}$ streptomycin. Cells were plated on coverslip-bottom 35 mm petri dishes (Cell E&G LLC), and grown for 1 day. On the day of the experiment, cells were serum starved in Lebovitz-15 (L-15) media (containing phenol red). Nanoruby colloid, devoid of large particles, was added to the cells at a final concentration of 25 $\mu g \cdot mL^{-1}$ in L-15, followed by incubation for 2 h. The cells were washed 3× with L-15 in preparation for TGP microscopy. Control cell samples not incubated with nanorubies were also prepared.

Images of the cells were acquired in brightfield to visualize the morphology and in PL mode to visualise bound nanorubies. 532 nm laser was used at a power of 132 mW (continuous wave) with a pulse width of 4 ms for epi-luminescence or 10 ms for TGP images. For TGP, Δt was fixed at 10 µs and a filter set #1 was used. The camera exposure time was set to 4 ms for epi-luminescence or 10 ms for TGP modes, with EM gain fixed at 100. Up to 25 images were collected for each cell at varying z-planes. These images were projected to form a single image by maximum pixel value in order to capture the best focal plane for individual nanorubies.

2.9 Nanoruby bioassay

Glass coverslips on glass-bottom-petri dishes (Cell E&G LLC) were biotinylated using a mixture of silane-PEG (20 mM, MW = 2 kDa, Laysan Bio Inc.) and silane-PEG-biotin (2 mM, MW = 3.4 kDa, Laysan Bio Inc.) prepared in Milli Q water. The coverslips were incubated for 2 hours at 40 °C to facilitate reliable biotinylation. Avidin (NeutrAvidin, Thermo Fisher Scientific) was added on the biotinylated coverslip. 1% (w/v) solution of BSA in PBS was used to block non-specific binding of nanorubies to the substrate/avidin. Biotinylated nanorubies were prepared at a concentration of 0.2 µg/mL in fetal bovine serum (Gibco, Thermo Fisher Scientific) and added to initiate binding. Live imaging was carried out by obtaining an image in every 10 s. The excitation laser power was optimised to minimise photodamage of streptavidin while limiting the compromise on the acquisition frame rate. For control experiments, the binding sites were blocked by adding 1 mM biotin (Sigma Aldrich) to the avidin-immobilised coverslip prior to adding biotinylated nanorubies.

3. Results and discussion

3.1 Nanoruby characterisation

The morphology of nanoruby sample was characterised by TEM. Analysis of TEM images showed a mean particle diameter of 70 ± 40 nm (Figure 3a). This value was obtained based on individual particle area measured by the image analysis, followed by spherical approximation. The mean hydrodynamic diameter of nanorubies in an aqueous colloid was measured by DLS as 80 ± 20 nm, as shown in Figure 3b. These values were obtained based on non-linear curve fitting of the size histograms to the inbuilt 'Extreme' peak function of Microcal Origin. The slight overestimation of hydrodynamic size measured by DLS with respect to physical size measured by TEM has been observed previously in other types of nanoparticles [34]. Aggregation of nanoparticles can also contribute to the increased hydrodynamic size, but we mitigated this effect by sonicating the samples before every measurement.

The PL excitation and emission spectra of the colloidal nanoruby are shown in Figure 3c. Two broad excitation peaks centred at 402 nm and 557 nm were observed and found identical to the peaks observed in bulk ruby [35]. A very narrow emission doublet, featuring two peaks at 690.6 nm and 692.1 nm, referred to as the R_1 and R_2 lines, originate from the transitions $\bar{E} \rightarrow {}^4A_2$ and ${}^2\bar{A} \rightarrow {}^4A_2$ of the Cr^{3+} colour-centres in ruby [36].

Using the time-gated photoluminescence microscopy (TGP), the PL lifetime of nanoruby, τ_{NR}, was estimated to be 3.7 ± 0.4 ms, as shown in Figure 3d. This value is comparable to the PL lifetime of bulk ruby reported elsewhere [37]. As mentioned earlier, such long lifetime makes nanorubies suitable for the time-gated imaging. Unlike the other promising PL nanomaterials, such as fluorescent nanodiamonds [38] and upconversion nanoparticles [39], nanoruby photoluminescence has been verified to be unaffected by environmental conditions, with no observed quenching effects [40].

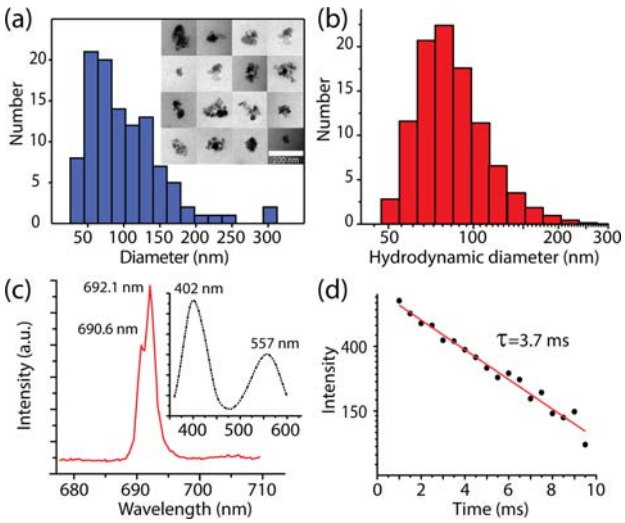

Figure 3 Histograms of nanoruby diameters measured by (**a**) TEM and (**b**) DLS. Inset in (**a**) presents images of 16 representative nanoruby particles. Scale bar, 200 nm. (**c**) Emission and excitation (inset) spectra of the as-produced nanoruby sample. (**d**) A semi-log plot of the photoluminescence intensity of nanoruby as a function of the time after the laser pulse. The solid line shows a single-exponential fit with τ_{NR} = 3.7 ms.

3.2 Single particle sensitivity by correlative imaging

A sample of discrete nanorubies sparsely dispersed on a gridded glass coverslip was imaged with our TGP microscope. As shown in Figure 4 (bottom panel), TGP imaging revealed a number of discrete spots. The full wave half maximum (FWHM) of these spots, dictated by the point-spread function (PSF) of the microscope optics, was measured as 400 ± 20 nm (Figure 4 inset). In the diffraction-limited case, the FWHM of the Airy disk intensity profile would measure approximately 320 nm, whereas our system exhibited a larger PSF. We interpret this width broadening to the objective lens aberrations (probably, uncorrected for the cover slip thickness). It is possible that the non-zero size of the nanorubies

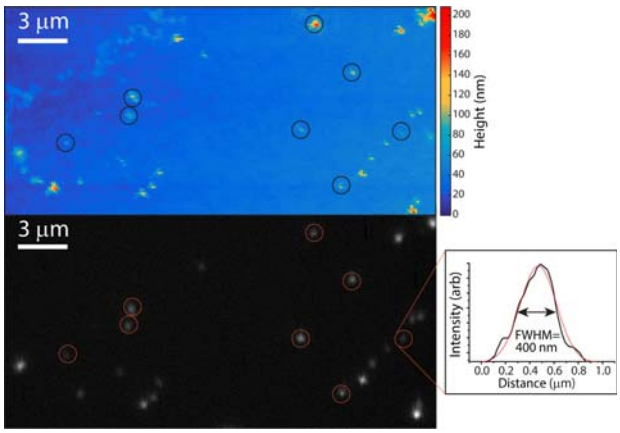

Figure 4 AFM (top) and TGP (bottom) images of discrete nanorubies deposited on a glass coverslip. The correlation between the AFM and TGP images is apparent, where circles indicate the corresponding particles matched between two images. (Inset) Intensity profile of one spot corresponding to a single 30 nm nanoruby (black), overlapped with a gaussian fit (red). The fit yielded an FWHM of 400 ± 20 nm.

might also explain the increased "apparent" point spread function of our imaging system. The assymetric profile of the recorded lateral PSF pointed to coma aberrations, which was more profound for off-centre objects. In order to confirm that these spots corresponded to discrete nanorubies, we analysed the same sample area by AFM to measure their heights at the nanometer scale (Figure 4, top panel). The TGP and AFM images of the discrete spots closely matched one another, both with respect to the positions and signal intensities of the circled particles. Nanorubies with height as small as 30 nm measured by AFM were clearly observable in the TGP image, confirming that the EMCCD-detected optical signal levels corresponded to individual nanorubies. For example, a signal level of 280 photons per second per pixel corresponded to a single nanoruby particle of diameter 30 nm (circled), as measured by the AFM.

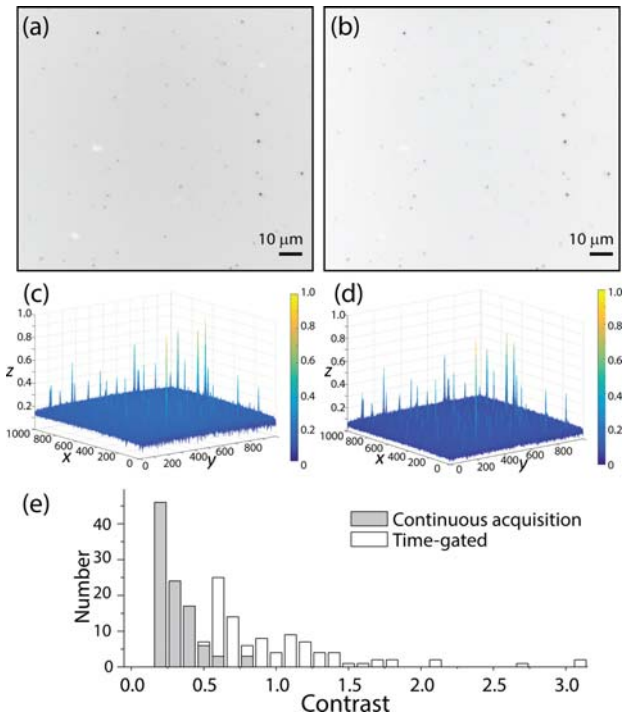

Figure 5 Optical images of nanorubies spin-coated on a glass coverslip acquired in (**a**) epi-luminescence and (**b**) TGP modes (Δt = 1000 μs) respectively using the filter set #1. Nanorubies appear as dark spots since the image is presented in an inverted brightness scale. (**c**) and (**d**) are the corresponding 3D-pseudo-colour plots after normalisation. The contrast enhancement in the TGP mode is especially evident in the 3D surface plots. (**e**) Histogram of the contrast values of discrete nanorubies imaged in epi-luminescence and TGP (Δt = 1 ms) modes. Details of image processing and calculation of contrast are described in Experimental section.

3.3 Photoluminescence contrast of nanorubies and the background of glass substrate

Representative PL images of nanorubies spin-coated on a glass coverslip (Section 2.2), captured in epi-luminescence (continuous excitation/detection) and TGP modes (Δt = 1000 μs) are presented in Figures 5a, b. The contrast of discrete nanorubies (C_{NR}) in the epi-luminescence imaging mode was inferior (≈ 25%) to that of the TGP mode (Figure 5e). Analysis of images acquired at smaller Δt values established that the photoluminescence of the BK7 glass substrate was a substantial contributor to the background observe in non-time gated images (B_s, where the subscript 's' denotes substrate). Since imaging of biological specimens frequently occurs on a glass

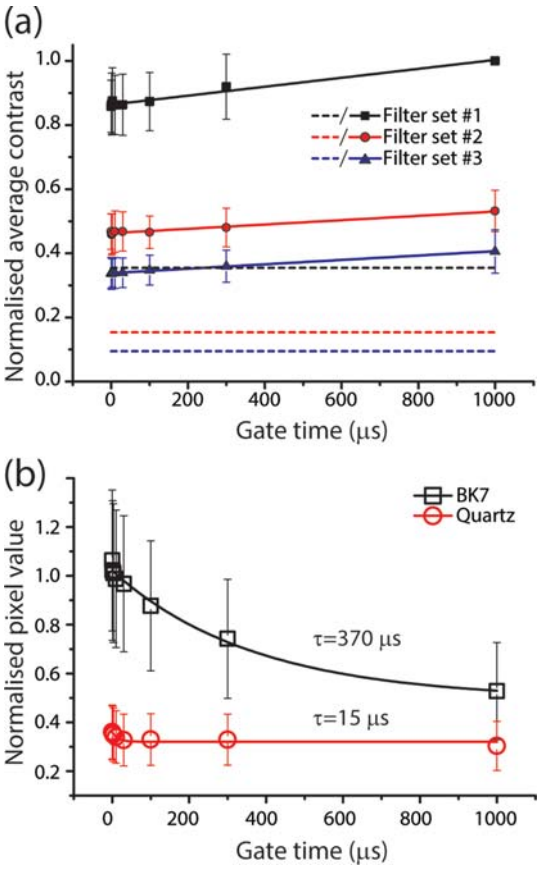

Figure 6 (**a**) A plot of the average contrast (C_{NR}) of discrete nanorubies placed on a BK7 glass coverslip, acquired in epi-luminescence (dashed lines) and TGP (data points fitted with solid lines) imaging modes, versus the gate time (not relevant for epi-luminescence imaging). Data sets represented by black squares, red circles and purple triangles were acquired using filter sets #1, #2 and #3 respectively. Lines are linear fits. (**b**) Temporal decay of optical signals from BK7 glass (open black squares) and quartz (open red circles) coverslips, expressed in terms of the pixel values. Solid lines represent single exponential fits.

slide or glass coverslip, it was worthwhile to investigate the glass substrate auto-photoluminescence and consider means of its suppression.

We compared spectral and time-gated methods to minimise B_s. Firstly, we attempted spectral discrimination. To this aim, three filter sets (Table 1), selected for suppression of a particular spectral range of B_s, were tested (Figure 6a). Secondly, we tested the time-gated discrimination. Here, the gate time, Δt was varied to analyse the effect of Δt on the contrast (Figure 6a). Lastly, we tested a non-auto-photoluminescent coverslip and slide made of fused quartz to reduce B_s (Figure 6b).

Figure 6a shows the C_{NR} of discrete nanorubies placed on a BK7 glass coverslip, as acquired in the epi-luminescence and TGP imaging modes plotted as a function of Δt. The filter set #1 demonstrated the best performance in terms of C_{NR} in both acquisition modes, while the set #3 displayed the worst performance. The filter set #1 transmitted the excitation and emission light with minimum losses; and it suppressed the auto-photoluminescence from the glass slide most efficiently, as shown in the transmission plot of the filter set #1 (Figure S1). The contrast enhancement in the TGP mode compared to the epi-luminescent mode was obvious for all three tested filter sets. The contrast increases with Δt, with values of 2.8, 3.5 and 4.4 fold for the filter sets #1, #2 and #3 respectively at $\Delta t = 1000$ µs (Figure 6a). Even though the filter set #3 showed the highest enhancement upon the time gating, the absolute contrast was the highest when using the filter set #1.

The PL lifetimes of the empty BK7 glass and quartz substrates, spectrally filtered by the filter set #1, are shown in Figure 6b. The lifetime of the BK7 glass was measured to be $(3.7 \pm 0.6) \times 10^2$ µs. The time trajectory of the optical signal originating from quartz coverslips exhibited a fast decay with a time constant of 15 ± 11 µs, which likely originates from the trailing edge of the laser excitation.

From these analyses, two observations are noteworthy. Firstly, the excitation laser light bleeding through the spectral filter sets represented a non-zero component of the B_s, as inferred by comparing the C_{NR} in the TGP and epi-luminescence modes (Figure 6). The suppression of this background component by routine spectral filtering can be difficult even in a carefully optimised setting, and practically impossible in macro-scale optical imaging of highly-scattering biological tissue [41]. The time-gated imaging mode provides an effective and inexpensive approach to completely eliminate this component. Secondly, the intrinsic photoluminescence of the BK7 glass, presumably originating from impurities, also contributed to B_s. Since these impurities were characterised by a relatively long τ_{PL} (Figure 6b), supressing this background was difficult by TGP imaging. At the same time, this contribution to the background was relatively low compared to that of biological autofluoresence (as seen below). Therefore, it is typically tolerable during optical imaging of biological samples, even when ultrahigh-sensitivity is desired. If this minimal background is untolerable, BK7 coverslips are to be replaced with quartz coverslips.

3.4 Time-gated imaging of single-nanorubies submerged in a fluorescent dye solution

In order to demonstrate the performance of the designed time-gated system, discrete nanorubies sparsely dispersed on a glass coverslip were submerged in a solution of a yellow-fluorescent organic dye. The results of the epi-luminescence and TGP imaging of this sample are shown in Figure 7. Despite the use of the filter set #1 (including a narrow, 23-nm wide, band-pass filter centred at 689 nm) optimised for the high-sensitivity detection of the nanoruby PL, the emission from the yellow dye subdued the nanoruby signal. However, in the TGP mode, the fluorescence signal from the yellow fluorescent dye was completely suppressed, which allowed for recovering the signal from discrete nanorubies. The background value of the signal from nanorubies in the dye solution is closely approached that of the EMCCD dark counts ($B_s = 5447 \pm 265$ count and Dark = 2972 ± 332 count)

3.5 Time-gated imaging of nanorubies in cells

The feasibility of using the TGP system to image nanorubies on a biological background of living cells was tested using cells (AtT-20, Section 2.8) incubated with nanorubies. Representative images of nanoruby-containing living cells, acquired in the bright

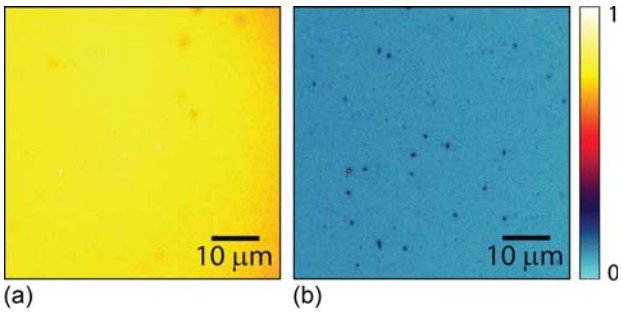

Figure 7 Images of nanorubies spin-coated on a glass coverslip and submerged in a solution of the yellow-fluorescent organic dye obtained by (**a**) epi-luminescence and (**b**) TGP imaging modes. Nanorubies are invisible in (**a**) whereas discrete nanorubies were clearly observed in (**b**).

field, epi-luminescence and TGP imaging modes are shown in Figure 8. In the TGP mode, the fluorescence originating from media and endogenous cell fluorophores (Figure 8b) is suppressed, resulting in background-free imaging of discrete nanorubies bound to the cell (Figure 8c).

This experimental configuration models a functional imaging scenario, where a fluorescent solution probe assays the functional state of the cell (e.g., intracellular Ca^{2+}) modulated by ligands such as neurotransmitters, while molecular trafficking of the receptor-bound ligands labelled with photoluminescent nanoparticles are visualised using the TGP mode. The nanoruby signal is confirmed by the control sample without nanorubies as shown in Figure 8 (a–c, right panel).

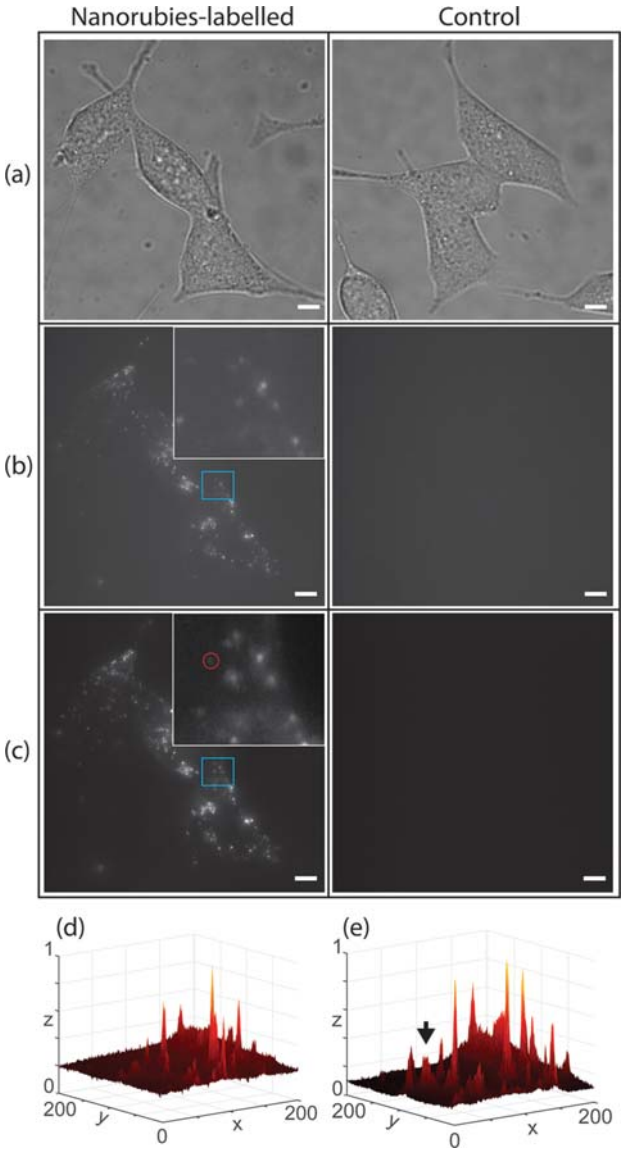

Figure 8 Microscopy images of AtT-20 cells. (**a**–**c**)Left and right columns: cells incubated with nanorubies and control, respectively. Rows: (**a**) Bright field, (**b**) epi-luminescence, and (**c**) TGP images. Insets in (**b**) and (**c**), blow-up images as framed by blue squares. A red circle marks the nanoruby indiscernible in (**b**). Scale bars in (**a**–**c**), 10 μm. (**d**) and (**e**) are normalised 3D-pseudo-colour plots of the epi-luminescence and TGP modes, respectively. The black arrow on (**e**) demarcates a representative peak which is only barely visible in (**d**).

3.6 *Single-molecule kinetic binding assay*

Detection of rare, but significant biomolecules or biological events in biological fluids, such as blood and urine, is known as "a needle in a haystack" prob-

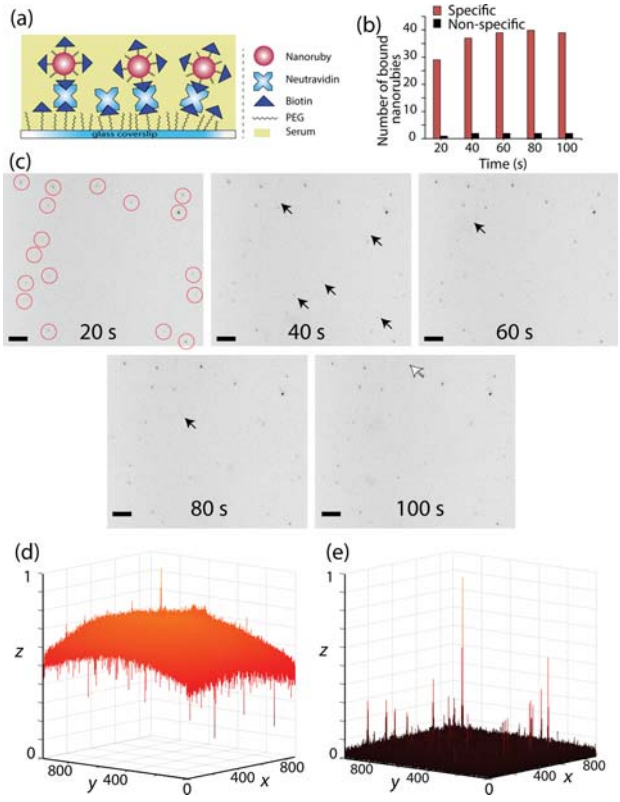

Figure 9 Schematic diagram of assaying antigens modelled by avidin with biotinylated nanorubies in serum. (**b**) A bar-chart of the number of nanorubies bound to the avidin-functionalised substrate, as a function of time, as observed in Video S2 and Video S3 (available in SI). Red and black bars represent specific and non-specific (negative control) binding. (**c**) Zoomed time-lapse images of the binding events (inverted color) captured from Videos S2 and S3. Red circles show nanorubies that had bound to the substrate before the start of video recording; black arrows show emerging bound nanorubies, a white arrow shows the detached nanoruby. Scale bar, 10 μm. (**d**) and (**e**) are normalised 3D-pseudo-colour plots of the epi-luminescence and TGP images, respectively.

lem, exacerbated by autofluorescence from endogenous flavins, nicotinamide adenine dinucleotides and porphyrins. Several assay formats and probes have been developed to detect clinically relevant proteins, nucelotides and other molecules (such as glucose) in biological fluids [42–44]. Here, we demonstrate our TGP method capability for a single-molecule kinetic assay, which is in our case modelled as an avidin-biotin pair in a biological fluid. We made use of nanorubies to label antigens modelled by avidin.

The binding of single biotinylated nanorubies to avidin in fetal bovine serum (serum) is schematised in Figure 9a. The binding was monitored over time and presented in Figure 9c, where black arrows mark newly bound nanorubies, while a white arrow shows the detachment of a weakly bound, presumably, adsorbed nanoruby from the coverslip. Video S2 (available in Supplementary Information file) shows the real time imaging of nanoruby kinetic binding, while Video S3 (see SI) shows the corresponding negative control assay, where few binding events registered.

The number of nanorubies bound to the immobilised avidin during the time series is presented in a bar chart in Figure 9b. Figure 9d and e, respectively, show epi-luminescence and TGP images of the specifically bound nanoruby distribution at the assay completion. In contrast with the epi-luminescent video microscopy, nanorubies were visualised clearly in the time-gated mode, thus showing the cutting-edge merit of the reported method. This demonstrates the feasibility of the method for assaying of molecular markers such as inflammatory markers or for bed-side monitoring of analytes in a clinical setting.

4. Conclusion

We demonstrate a time-gated photoluminescence microscopy system that enables fast and ultrahigh-sensitivity imaging of long-lifetime photoluminescent probes in optically crowded environments for extended periods of time. Time-gated imaging of nanoruby photoluminescence enabled its separation from short-lived laser scatter, autofluorescence of biological matter and organic fluorescent probes. By using time-gated imaging mode, we have been able to demonstrate the detection of single nanorubies dispersed on a coverslip, even when they were submerged in a solution of organic fluorescent dye, or bound to cells submerged in a fluorescent culture medium. The rapid imaging capability of the system enabled live monitoring of single particle binding events in autofluorescent biological fluids.

The presented results demonstrate the potential of nanorubies as molecular probes or labels for a range of applications in the life sciences, such as real-time assaying of analytes in biological fluids. These developments will offer new opportunities for visualising intracellular molecular trafficking and detecting rare biomolecular events in an optically crowded background of cells and tissues.

Supporting Information

Additional supporting information may be found in the online version of this article at the publisher's website.

Acknowledgements We acknowledge support of the Federal targeted program of the Russian Federation, Grant number RFMEFI57814X0030. The authors thank Mr. Russell Field, Dept. of Environmental Sciences, Macquarie University for his assistance with DLS Mastersizer 2000 equipment.

Author biographies Please see Supporting Information online.

References

[1] J. W. Lichtman and J.-A. Conchello, Nat. Methods **2**, 910–919 (2005).
[2] M. P. Backlund, M. D. Lew, A. S. Backer, S. J. Sahl, and W. Moerner, ChemPhysChem **15**, 587–599 (2014).
[3] J. R. Lakowicz, Principles of Fluorescence Spectroscopy, 3rd edition ed. (Springer, New York), (2006).
[4] M. J. Ruedas-Rama, J. D. Walters, A. Orte, and E. A. Hall, Anal. Chim. Acta **751**, 1–23 (2012).
[5] V. K. A. Sreenivasan, A. V. Zvyagin, and E. M. Goldys, J Phys Condens Matter **25**, 194101 (2013).
[6] P. Sharma, S. Brown, G. Walter, S. Santra, and B. Moudgil, Adv Colloid Interface Sci **123–126**, 471–485 (2006).
[7] W. E. Moerner, Proc. Natl. Acad. Sci. U.S.A. **104**, 12596–12602 (2007).
[8] W. Kong, R. Liu, H. Li, J. Liu, H. Huang, Y. Liu, and Z. Kang, J. Mater. Chem. B **2**, 5077–5082 (2014).
[9] L. Zhang and E. Wang, Nano Today **9**, 132–157 (2014).
[10] P. Zhang, X. X. Yang, Y. Wang, N. W. Zhao, and C. Z. Huang, Nanoscale **6**, 2261–2269 (2014).
[11] S. W. Wu, G. Han, D. J. Milliron, S. Aloni, V. Altoe, D. V. Talapin, B. E. Cohen, and P. J. Schuck, Proc. Natl. Acad. Sci. U.S.A. **106**, 10917–10921 (2009).
[12] A. M. Edmonds, M. A. Sobhan, V. K. A. Sreenivasan, E. A. Grebenik, J. R. Rabeau, E. M. Goldys, and A. V. Zvyagin, Part Part Syst Charact **30**, 506–513 (2013).
[13] K. Y. Han, K. I. Willig, E. Rittweger, F. Jelezko, C. Eggeling, and S. W. Hell, Nano Lett. **9**, 3323–3329 (2009).

[14] Z. Yi, W. Lu, Y. Xu, J. Yang, L. Deng, C. Qian, T. Zeng, H. Wang, L. Rao, H. Liu, and S. Zeng, Biomaterials **35**, 9689–9697 (2014).
[15] E. Dimitrow, I. Riemann, A. Ehlers, M. J. Koehler, J. Norgauer, P. Elsner, K. König, and M. Kaatz, Exp. Dermatol. **18**, 509–515 (2009).
[16] M. S. Roberts, M. J. Roberts, T. A. Robertson, W. Sanchez, C. Thörling, Y. Zou, X. Zhao, W. Becker, and A. V. Zvyagin, J Biophotonics, **1**, 478–493 (2008).
[17] M. Y. Berezin and S. Achilefu, Chem. Rev. **110**, 2641–2684 (2010).
[18] D. J. Gargas, E. M. Chan, A. D. Ostrowski, S. Aloni, M. V. P. Altoe, E. S. Barnard, B. Sanii, J. J. Urban, D. J. Milliron, and B. E. Cohen, Nat Nanotechnol **9**, 300–305 (2014).
[19] R. M. Rich, D. L. Stankowska, B. P. Maliwal, T. J. Sørensen, B. W. Laursen, R. R. Krishnamoorthy, Z. Gryczynski, J. Borejdo, I. Gryczynski, and R. Fudala, Anal Bioanal Chem **405**, 2065–2075 (2013).
[20] E. A. Grebenik, A. Nadort, A. N. Generalova, A. V. Nechaev, V. K. Sreenivasan, E. V. Khaydukov, V. A. Semchishen, A. P. Popov, V. I. Sokolov, and A. S. Akhmanov, J Biomed Opt **18**, 076004 (2013).
[21] Y. Y. Hui, L.-J. Su, O. Y. Chen, Y.-T. Chen, T.-M. Liu, and H.-C. Chang, Sci Rep **4**, 5574-1–5574-7 (2014).
[22] G. Mandal, M. Darragh, Y. A. Wang, and C. D. Heyes, Chem. Commun. **49**, 624–626 (2013).
[23] L. Zhang, X. Zheng, W. Deng, Y. Lu, S. Lechevallier, Z. Ye, E. M. Goldys, J. M. Dawes, J. A. Piper, and J. Yuan, Sci Rep **4**, 6597-1–6597-6 (2014).
[24] L. Tian, Z. Dai, L. Zhang, R. Zhang, Z. Ye, J. Wu, D. Jin, and J. Yuan, Nanoscale **4**, 3551–3557 (2012).
[25] B. Valeur, M. N. Berberan-Santos, Molecular fluorescence: principles and applications (John Wiley & Sons, 2012).
[26] R. Connally, D. Jin, and J. Piper, Cytometry Part A **69**, 1020–1027 (2006).
[27] S. Bouccara, E. Giovanelli, G. Sitbon, N. Lequeux, T. Pons, V. Loriette, and A. Fragola, Proc. SPIE Int. Soc. Opt. Eng. **8947**, 89471B-1–89471B-8 (2014).
[28] R. Frischknecht, M. Heine, D. Perrais, C. I. Seidenbecher, D. Choquet, and E. D. Gundelfinger, Nat. Neurosci. **12**, 897–904 (2009).
[29] W. A. W. Razali, V. K. A. Sreenivasan, E. M. Goldys, and A. V. Zvyagin, Langmuir **30**, 15091–15101 (2014).
[30] A. Nadort, V. K. Sreenivasan, Z. Song, E. A. Grebenik, A. V. Nechaev, V. A. Semchishen, V. Y. Panchenko, and A. V. Zvyagin, PloS one **8**, e63292 (2013).
[31] C. Bradac, T. Gaebel, C. Pakes, J. M. Say, A.V. Zvyagin, and J. R. Rabeau, Small **9**, 132–139 (2013).
[32] E. Peli, J Opt Soc Am A Opt Image Sci Vis **7**, 2032–2040 (1990).
[33] P. Whittle, Vision Res. **26**, 1677–1691 (1986).
[34] M. A. Dobrovolskaia, A. K. Patri, J. Zheng, J. D. Clogston, N. Ayub, P. Aggarwal, B. W. Neun, J. B. Hall, and S. E. McNeil, Nanomedicine **5**, 106–117 (2009).
[35] M. B. Walter Koechner, Solid-State Lasers: A Graduate Text (Springer, New York Berlin Heidelberg, 2002).
[36] C. Pflitsch, R. Siddiqui, and B. Atakan, Appl Phys A Mater Sci Process **90**, 527–532 (2008).
[37] D. E. Chandler, Z. K. Majumdar, G. J. Heiss, and R. M. Clegg, J Fluoresc **16**, 793–807 (2006).
[38] F. A. Inam, M. D. Grogan, M. Rollings, T. Gaebel, J. M. Say, C. Bradac, T. A. Birks, W. J. Wadsworth, S. Castelletto, and J. R. Rabeau, ACS nano **7**, 3833–3843 (2013).
[39] J. Zhao, D. Jin, E.P. Schartner, Y. Lu, Y. Liu, A.V. Zvyagin, L. Zhang, J. M. Dawes, P. Xi, and J. A. Piper, Nat Nanotechnol **8**, 729–734 (2013).
[40] W. Q. Zhang, W. Razali, V. Sreenivasan, T. M. Monro, and D. Taylor, Universal optical fibre fluoresence sensing platform for wine monitoring, in: 40th Australian Conference on Optical Fibre Technology, Adelaide, Australia (2015).
[41] F. Leblond, S. C. Davis, P. A. Valdés, and B. W. Pogue, J. Photochem. Photobiol. B, Biol. **98**, 77–94 (2010).
[42] J. Li, W. Zhou, X. Ouyang, H. Yu, R. Yang, W. Tan, and J. Yuan, Anal. Chem. **83**, 1356–1362 (2011).
[43] X. Meng, M. Xu, J. Zhu, H. Yin, and S. Ai, Electrochim. Acta **71**, 233–238 (2012).
[44] Y. He, H.-F. Wang, and X.-P. Yan, Anal. Chem. **80**, 3832–3837 (2008).